CrossMark

RESEARCH ARTICLE

Heat Flux in the Strong-Wind Nocturnal Boundary Layer

L. Mahrt[1] (ORCID)

Abstract Sonic anemometer measurements are analyzed from two primary field programs and 12 supplementary sites to examine the behaviour of the turbulent heat flux near the surface with high wind speeds in the nocturnal boundary layer. On average, large downward heat flux is found for high wind speeds for most of the sites where some stratification is maintained in spite of relatively intense vertical mixing. The stratification for high wind speeds is found to be dependent on wind direction, suggesting the importance of warm-air advection, even for locally homogenous sites. Warm-air advection is also inferred from a large imbalance of the heat budget of the air for strong winds. Shortcomings of our study are noted.

Keywords Heat flux · Nocturnal boundary layer · Stable boundary layer ·
Stratified turbulence · Topography

1 Introduction

The windy nocturnal boundary layer generally obeys similarity theory, so that recently more attention has been devoted to the weak-wind very stable boundary layer. Traditionally, the nocturnal boundary layer under windy conditions is expected to be near-neutral because the stratification is seriously reduced by the relatively intense vertical mixing, which limits the downward heat flux.

From another point of view, the heat flux can be posed in terms of a maximum sustainable heat flux, which increases with increasing wind speed (Van de Wiel et al. 2012; Donda et al. 2016) or increasing wind shear (Van Hooijdonk et al. 2015). For high wind speeds the actual heat flux is expected to decrease with increasing wind speed because the strong mixing reduces both the stratification and temperature fluctuations. With this expectation, surface radiative cooling cannot maintain significant stratification.

Stratification, however, may be maintained in cases of warm-air advection even though microscale horizontal gradients might be minimized in windy conditions. For a given larger-

---

✉ L. Mahrt
  mahrt@nwra.com

[1] NorthWest Research Associates, 2171 NW Kari Pl, Corvallis, OR 97330, USA

scale horizontal gradient of temperature, the temperature advection increases with wind speed. Boundary-layer studies have often implied important temperature advection, but estimating the horizontal temperature gradient from measurements is difficult and often varies significantly with the horizontal scale of the calculation. Most studies of advection have concentrated on drainage flows (Sun 2007; Oliveira et al. 2012) or on horizontal temperature gradients forced by abrupt changes in surface roughness and heat flux (Garratt 1990). Increased spatial variation with increasing stability was quantified in the numerical simulations of Stoll and Porté-Agel (2009).

Sterk et al. (2016) assessed the potential importance of advection by comparing numerical model results with observations over snow surfaces. Bonin et al. (2015) observed development of stratification in the overlying residual layer with higher wind speeds, consistent with the larger-scale horizontal temperature gradient and the inferred increase of warm-air advection with height. Nakamura and Mahrt (2006) analyzed the heat budget of the air near the surface and contrasted the role of the inferred temperature advection between sites. Vosper et al. (2013) numerically simulated flow in an instrumented valley and found important complex advection of temperature.

Our study reexamines the windy stable boundary layer by using two primary datasets and a number of additional auxilliary datasets with different types of vegetation and terrain. When does the heat flux and stratification vanish with strong winds? How does the advection of temperature influence the stratification and heat flux in the windy stable boundary layer? Can we sort out the influences of wind speed, surface radiative cooling and advection on the surface heat flux?

2 Measurements

We concentrate on the analysis of sonic anemometer measurements at 1-m height from two field programs, which are now briefly described.

2.1 FLOSSII

Seven levels of Campbell CSAT sonic anemometers were deployed on a 30-m tower in North Park, Colorado, USA, during the Fluxes Over a Snow Surface II experiment (FLOSSII, http://www.eol.ucar.edu/isf/projects/FLOSSII/) from 20 November 2002 to 2 April 2003. This site was located within a broad, deep valley (Mahrt and Vickers 2005), with the surface consisting of matted grass, occasionally with a shallow snow cover. For the prevailing southerly and south-westerly wind directions, the grass yielded to brush upwind 100–200 m from the site.

The sonic anemometer data are not tilt-rotated because we suspect that some mean vertical motion might be real due to the upwind change of roughness, and flow acceleration over the matted grass (at least 100 m in all directions) would lead to subsidence. In this case, removal of the vertical motion by rotation of the coordinate system would not be justified. The net radiation is computed as the difference between the upward and downward longwave radiation measured by Epply pyrgeometers.

2.2 Shallow Cold Pool Experiment

The Shallow Cold Pool (SCP) experiment was conducted over semi-arid grasslands in northeastern Colorado, USA from 1 October to 1 December 2012. Details can be found at https://www.eol.ucar.edu/field_projects/scp and in Mahrt and Thomas (2016), which includes a

map of the 21 stations. The main valley is relatively small, roughly 12 m deep and 270 m across. The study concentrates on the measurements from station A1, which is outside the valley on relatively flat terrain and is upwind from the valley for the accepted wind directions. The stratification is computed from 1-Hz temperature measurements from NCAR hygrothermometers deployed at 0.5 and 2 m. For the high plains SCP site, windy conditions were commonly observed, and only a few nights were entirely clear with many nights partly cloudy. The nocturnal net radiation was computed from the longwave components measured by a Kipp and Zonen CG4 pyrgeometer at 1.5 m, located 17 m south-east (147°) from the main tower. Although, the net radiation measurements are separated from station A1 by approximately 800 m, the sparse vegetation is similar at both locations.

2.3 Restrictions

The FLOSSII site will be emphasized for analysis of the heat budget of the air because the SCP tower is in a shallow valley with more complex vertical structure, and the length of the dataset from the SCP field program is two months, compared with four months for the FLOSSII field program. We report results from the SCP site when they differ systematically from those of the FLOSSII site.

We use the net radiation at the surface, R_{net}, defined as the difference between the downward and upward longwave radiative fluxes. For part of the analyses, the observations are screened using the requirement of significant net radiative cooling ($-R_{net} > 20$ W m^{-2}) to exclude cloudy conditions, and this threshold value is chosen in Sect. 5. Cases of positive nocturnal R_{net} during the night are uncommon and are associated with a relatively warm cloud cover. The radiation components are available only as 5-min averages that are then projected onto 1-min intervals. For the current datasets, the difference between the sensible heat flux and the sonic virtual heat flux is negligible, and no corrections were made. For these two sites, the stratification, $\delta\theta$, is computed as the difference of potential temperature between the 0.5- and 2-m levels.

The analysis includes only the time period between 2000 LST and 0500 LST on the following day in order to exclude sunrise and the evening transition period. Several of the relationships examined here are significantly altered during the complex rapidly cooling transition period, which will be investigated in a separate study.

2.4 Other Field Programs

Twelve supplementary datasets are included for nominal investigation of the dependence of the heat flux on the wind speed; see Table 1 for details. Many of these datasets do not include adequate measurements near the surface to confidently evaluate the stratification. In addition, the datasets are processed differently using measurements from levels that differ between the field programs. The datasets over land represent nocturnal conditions while the marine datasets are based on cases of downward heat flux.

The BPP site (Thomas et al. 2012) is located on the Botany and Plant Pathology Farm of Oregon State University, and the observations analyzed here were collected from late August until mid October 2011. The site is flat but locally heterogeneous with mixed grass fields, orchards and vineyards. The computation of $\delta\theta$ and other processing procedures are summarized in Mahrt and Thomas (2016). A central tower allows evaluation of the heat flux budget of the air.

Observations in CASES-99 (Cooperative Atmospheric Surface Exchange Study) (Poulos et al. 2001; Sun et al. 2002) were collected over grassland in south central Kansas, USA.

Table 1 Twelve supplementary datasets

Site	Sfc.	Duration	Height (m)	References
BPP	Grass	2 months	1	Thomas et al. (2012)
OHATS	Coastal	2 months	5	Kelly et al. (2009)
Eyerly	Burned pine	2 years	10	Schwarz et al. (2004)
Juniper	3-m juniper	9 months	11	Schwarz et al. (2004)
Intermediate pine	13-m ponderosa	5 years	6.1	Schwarz et al. (2004)
Falster	24-m beech	2 months	33	Dellwik and Jensen (2000)
CASES-99	Grass	1 months	1	Poulos et al. (2001)
CBLAST	Coastal zone	2 months	6	Edson et al. (2007)
EBEX	Cotton, etc.	1 months	2	Oncley et al. (2007)
Alaska	Snow	3 months	2	None
SMACEX	Crops	3 months	2	Kustas et al. (2004)
NEAQS	Coastal zone	1 month	17.5	Fairall et al. (2006)

The columns identify the field program, surface type, duration, height of the primary level above the ground surface or above the vegetation top and a citation for instrument descriptions

This dataset is of 1-month duration but has become the standard for analysis of the nocturnal boundary layer. A 60-m tower allows evaluation of the heat flux budget of the air.

We also analyze measurements from 14 eddy-correlation towers in the Soil Moisture Atmosphere Coupling Experiment (SMACEX) over farmland in central Iowa, USA, mainly soybeans and corn. Station spacing is on the order of 1 km or greater, and data were collected at roughly 2 m above the crop canopy. Two of the 16 stations were eliminated because of local heterogeneity or instrumental issues. We also analyze sonic anemometer measurements over a uniform beech forest that were collected on Falster Island, Denmark, from 23 February to 29 April 1994, at 33 m above the 24-m high canopy. We additionally analyze eddy-correlation measurements from three sites in central Oregon, USA (Table 1) based on CSAT-3 sonic anemometers deployed at 6.1 m above a 15-m mature ponderosa pine forest, 11 m above the surface of a 3-m sparse juniper forest and 10 m over a largely burned area (Table 1). These sites are described in Schwarz et al. (2004).

Additionally, we analyze eddy-correlation data collected from Point Barrow, Alaska, USA, from March through May 2005 with a CSAT3 sonic anemometer at 2 m over flat snow-covered short tundra. A small portion of the data occur with penetration of sedge shoots with tussocks 0.1–0.2 m above the snow.

NEAQS-04 observations were collected on the NOAA research vessel Ronald H. Brown in the Gulf of Maine during July and August of 2004. The observations for wind speed $V < 4.5$ m s^{-1} have been omitted because the 17.5-m level of the sonic anemometer was thought to be too high to approximate the surface fluxes in a shallow stable boundary layer (Fairall et al. 2006). Observations from the Air–Sea Interaction Tower (ASIT) were collected during the CBLAST Weak Wind experiment from late July to early August 2003. The offshore tower is located about 3 km south of Martha's Vineyard where the water depth is 15 m. Here, we analyze data from the CSAT3 sonic anemometer measurements at approximately 6 m above the average level of the water surface. The Ocean Horizontal Array Turbulence Study (OHATS) included two arrays of sonic anemometers located 5 and 5.58 m above the sea surface; the sonic anemometers were horizontally separated by only 0.6 m. For the more

homogeneous networks or sonic arrays (OHATS, SMACEX, EBEX), we have averaged the wind components and the heat flux over all of the sonic anemometers.

The FLOSSII dataset is the primary dataset for our analyses with significant additional use of the SCP dataset. The BPP and CASES-99 datasets provide additional information where the calculation of the stratification is reliable, and where the data processing is similar to that for the FLOSSII and SCP measurements.

2.5 Averaging

The flow is partitioned as

$$\phi = \phi' + \overline{\phi}, \tag{1}$$

where the overbar designates a time average at a fixed point, ϕ is one of the transported variables such as potential temperature or one of the velocity components, $\overline{\phi}$ is the average over the averaging time τ, and ϕ' is the deviation from such an average. The vertical heat flux for a given averaging window is then computed as $\overline{w'\theta'}$, where w' is the vertical velocity fluctuation and θ' is the fluctuation of potential temperature. Choice of averaging times are based on multi-resolution heat cospectra and are discussed in more detail in Mahrt and Thomas (2016) and references therein. Acevedo and Mahrt (2010) explicitly discuss the cospectra and sensitivity to the averaging length for the FLOSSII data. Our study uses a 1-min averaging time for all of the datasets. The heat flux on time scales >1 min for the FLOSSII SCP and BPP sites varies in sign and, on average, does not contribute significantly to the heat flux even for stronger wind speeds. Other datasets were not checked for the dependence of the heat flux on scale.

2.6 Bin Averaging

For some of the analyses, we average turbulence quantities over intervals of an independent variable (bin averaging) such as wind speed, as discussed in more detail in Mahrt and Thomas (2016). Our analyses also include bivariate bin averaging (Williams et al. 2013) corresponding to the average of all of the values of the heat flux that simultaneously occur for a specific interval of $\delta\theta$ and a specific interval of V. The standard errors for bin averaging are generally quite small compared to the variation between bins because of the very large number of samples. However, the uncertainty indicated by the standard error might be significantly underestimated because the assumption of independence between the 1-min windows is occasionally violated.

2.7 Stability

The stability is expressed in terms of the bulk Richardson number

$$Rb \equiv \sqrt{\frac{gz\delta\theta}{\Theta V^2}}, \tag{2}$$

where g is the acceleration due to gravity and z is the height of the wind measurement above the ground (Table 1). The gradient Richardson number is typically an order of magnitude greater and varies more erratically than the bulk Richardson number.

3 Budget

3.1 Basic Equations

The heat budget of the air can be expressed as

$$\frac{\partial \overline{\theta}}{\partial t} + \mathbf{V} \cdot \nabla \overline{\theta} = -\frac{\partial \overline{w'\theta'}}{\partial z} - \frac{\partial \overline{u'\theta'}}{\partial x} - \frac{\partial \overline{v'\theta'}}{\partial y} + R_*, \tag{3}$$

where θ is potential temperature, $\mathbf{V}$ is the horizontal wind vector, u is the horizontal velocity component directed toward the east, v is the horizontal velocity component directed toward the north, and R_* represents other terms such as the clear-air radiative flux divergence (Hoch et al. 2007; Edwards 2009).

Several simple idealized (prototype) flows can be constructed after neglecting R_* and the horizontal flux-divergence terms. For homogenous conditions where the advection vanishes,

$$\frac{\partial \overline{\theta}}{\partial t} \approx -\frac{\partial \overline{w'\theta'}}{\partial z}, \tag{4}$$

such that local cooling is caused entirely by the turbulent heat-flux divergence. An advective balance is defined for cases with strong horizontal heterogeneity such that the advection is significantly larger than the local time variations, in which case

$$\mathbf{V} \cdot \nabla \theta \approx -\frac{\partial \overline{w'\theta'}}{\partial z}. \tag{5}$$

With this *quasi-stationary regime* where the local time change is small, advection distorts the profile of the heat flux as observed by Mahrt and Vickers (2005) and studies cited therein. For example, cold-air advection in Eq. 5 must be balanced by heat-flux convergence such that the downward heat flux increases with height in the layer of horizontal advection, implying a maximum at some overlying level. Although this balance may never occur in pure form, it could lead to considerable distortion of the flux profile.

If local changes are almost entirely due to advection (isentropic flow) rather than the flux divergence,

$$\frac{\partial \overline{\theta}}{\partial t} \approx -\mathbf{V} \cdot \nabla \theta. \tag{6}$$

Some of the flow situations observed below approach one of the simplified versions of Eq. 3.

3.2 Evaluation of Advection and Horizontal Flux Divergence Terms

Horizontal transport occurs on a continuum of scales, and averaging attempts to partition the transport into that carried by turbulent fluctuations and that carried by the larger-scale, non-turbulent motions. With respect to Eq. 3, the turbulence is computed as deviations from a time average at a fixed station, and the larger scale transport appears as advection, which is proportional to the gradient of $\overline{\theta}$. The evaluation of the horizontal gradient from the network measurements introduces a horizontal length scale based on the spacing between stations. If the station spacing is significantly larger than the largest turbulent eddies, then horizontal transport by the smallest scale non-turbulent motions is not captured. Because Taylor's hypothesis is a poor approximation for the small non-turbulent motions (Mahrt et al. 2009), the conversion between time scales defined by the time averaging at individual stations and space scales defined by the network is not possible.

In addition, temperature differences between adjacent stations or differences across the entire network may be too small to measure, yet may correspond to significant temperature advection. For example, with a large value of V of 10 m s^{-1}, the difference of $\overline{\theta}$ across a 300-m distance (rough domain size for the 21 stations) that would be required to produce $\partial\overline{\theta}/\partial t = 1$ K h^{-1} is only about 0.01 K, which is not measurable. Thus, advection cannot be estimated from the SCP network for large V, and adequate measurements were not available on larger scales. The FLOSSII site included only three stations spaced roughly 1-km apart, which is insufficient for assessing advection. Mean vertical motions from sonic anemometers are unreliable (Vickers and Mahrt 2006) so that vertical advection cannot be estimated.

The horizontal turbulent flux of θ and its spatial distribution across the SCP network is noisy. However, after averaging results for a given wind direction sector, a spatial pattern over the gentle topography emerges. The averaged horizontal flux-divergence term can be on the order of 0.2 K h^{-1}, which is small but still significant. However, the accuracy of such estimates remains uncertain, and so we do not use the uncertain direct estimates of advection and horizontal heat flux divergence.

### 3.3 Heat Budget Evaluated from the Observations

Only $\partial\overline{\theta}/\partial t$ and $-\partial\overline{w'\theta'}/\partial z$ can be estimated from the measurements with any certainty. In the analysis below, the relative importance of the advection is tentatively inferred from the residual of the heat budget. The temperature tendency is evaluated using a moving two-point differencing approach described in Mahrt and Thomas (2016).

The flux divergence averaged over the field program increases slowly with increasing averaging time, τ, up to $\tau \approx 1$ min. Because the temperature tendency is linear, its value after averaging over many samples is not sensitive to τ. The flux-divergence and tendency terms increase when evaluated over a thinner layer adjacent to the ground compared to a deeper layer, but the budget imbalance and its qualitative dependence on V does not depend on the exact choice of the layer.

For "moderate and stronger" 1-m wind speeds in the FLOSSII measurements ($V > 3$ m s^{-1}), the cooling due to the flux divergence is large, roughly 4.5 K h^{-1} (Fig. 1, black). The averaged observed temperature tendency, $\partial\theta/\partial t$, is small ($< 1$ K h^{-1}) mainly because the evening transition period with rapid cooling is not included in the calculation. This implies that the flux divergence is balanced primarily by warm-air advection belonging to the "advective balance" regime (Eq. 5). The inferred warm-air advection for stronger winds is found to be consistent with the advection inferred from the relationships between the heat flux, stratification and wind direction (Sect. 6).

For the weakest winds ($V < 1$ m s^{-1}), the vertical heat-flux convergence is a small warming term while in actuality weak cooling is observed ($\partial\overline{\theta}/\partial t < 0$). If these terms are not dominated by errors, the imbalance between the flux-divergence and tendency terms implies cold-air advection and the inferred cold-air advection could be, at least in part, related to local drainage flows. The tower at the FLOSSII site is located in a shallow valley with a very small down-valley slope although more significant slopes begin about 1 km from the site.

The heat budget of the air and inferred advection are more complex at the SCP, BPP and CASES-99 sites. For all three tower sites, the flux-divergence terms and inferred advection are generally large compared to the temperature tendency. The following discusses results for the FLOSSII measurements, with the results similar for the smaller SCP dataset except where noted.
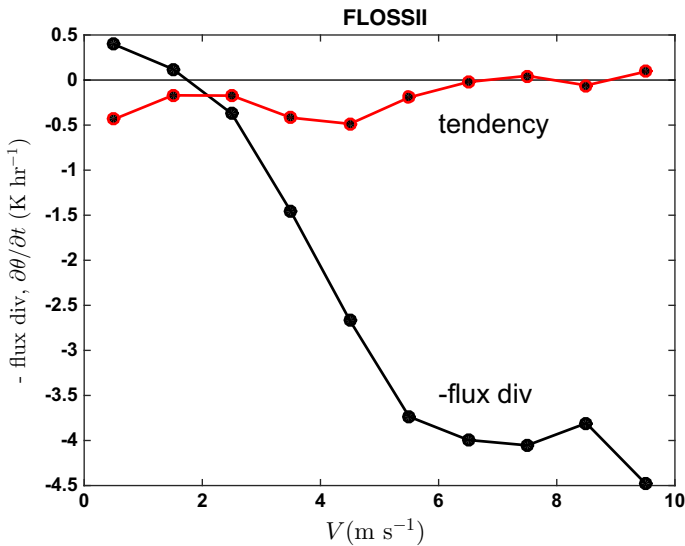
Fig. 1 The averaged heat-flux divergence term (*black*) and the local warming (*red*) for different intervals of V based on bin averaging of the 1-min values for the FLOSSII site for $-R_{\text{net}} > 20$ W m^{-2}. The heat-flux divergence is evaluated between the 0.5-m to 10-m observational levels. V and $\partial\theta/\partial t$ are evaluated at 5 m

4 Dependence of the Heat Flux on V and $\delta\theta$

The bulk transfer relationship motivates some of the analyses herein although we do not directly evaluate this. The bulk relation can be written as

$$\overline{w'\theta'} = -C_H V \delta\theta, \tag{7}$$

where C_H is the bulk transfer coefficient for heat. Thus, the heat flux is assumed to be proportional to V and $\delta\theta$. Normally, C_H is considered to be a function of R_b and thus a function of V and $\delta\theta$. However, evaluation of this function is sensitive to the method of analysis, the occurrence of ratios with very small denominators, and self-correlation due to the shared variables between C_H and R_b. Here we simply investigate the dependence of the heat flux on V and $\delta\theta$ without considering similarity theory or the stability dependence of C_H.

4.1 Wind-Speed Dependence

Relating the heat flux to V alone is dimensionally inconsistent but of historical interest. Because $\delta\theta$ is often strongly inversely correlated with V, the wind speed is the best single predictor of the heat flux. For the FLOSSII site, $\delta\theta$ systematically decreases with increasing V up to $V \approx 5$ m s^{-1} (Sect. 5; Fig 6a).

For the FLOSSII site, the downward heat flux increases slowly with increasing V until V reaches a threshold of about 1.5 m s^{-1} and then increases more rapidly with increasing V (Fig. 2a). Sun et al. (2012) examined this threshold velocity expressed in terms of various turbulence quantities. This threshold has been examined in a number of other recent studies (e.g. Van de Wiel et al. 2012; Acevedo et al. 2015).
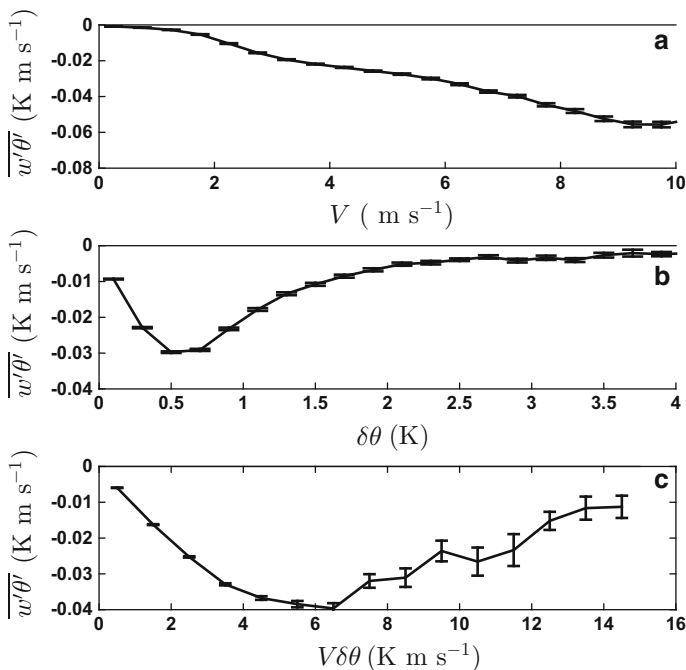
Fig. 2 The dependence of $\overline{w'\theta'}$ on: **a** V, **b** $\delta\theta$ and **c** $V\delta\theta$ for the FLOSSII site

This threshold V appears to some degree in all of the datasets considered here (Fig. 3). Significant differences are observed between sites partly due to different surface conditions, surface heterogeneity, different roles of advection, and different measurement heights and processing. For this reason, we interpret Fig. 3 mainly in terms of overall dependencies without attention to detailed quantitative differences between sites. Although V never completely reaches zero, the magnitude of the heat flux appears to remain non-zero with zero V particularly at the Falster site, at all of the complex terrain sites except SCP A1, and at the OHATS site. For very small V, turbulence and heat flux could be generated by non-stationary, non-turbulent motions for very stable conditions that are not resolved by the calculation of V based on the 1-min averaging windows.

The downward heat flux increases with increasing V at least up to $V = 10\ \mathrm{m\ s^{-1}}$ for almost all of the sites (Fig. 3a). For $V > 10\ \mathrm{m\ s^{-1}}$ (not shown), most of the sites have inadequate data and/or show less systematic dependence of the heat flux on V. The large values of the downward heat flux for larger V often exceed the magnitude of the surface net radiation. For the CASES-99 site, the downward heat flux actually decreases for large V (Fig. 3a, green line) as can be anticipated from Fig. 7 in Sun et al. (2016). Large V values at the CASES-99 site often occur with northerly flow and possible cold-air advection.

The increase of the downward heat flux with increasing V occurs for all of the other sites whether the site is on relatively flat terrain (Fig. 3a), in complex terrain (Fig. 3b), or over the sea (Fig. 3c). The dependence of the heat flux on V is more similar between the different complex terrain sites than between the sites over flatter land, suggesting that topography is an important influence. The EBEX and Alaska sites are considered to be flat terrain sites although the EBEX site is within 50 km of low mountains with typical heights of a few
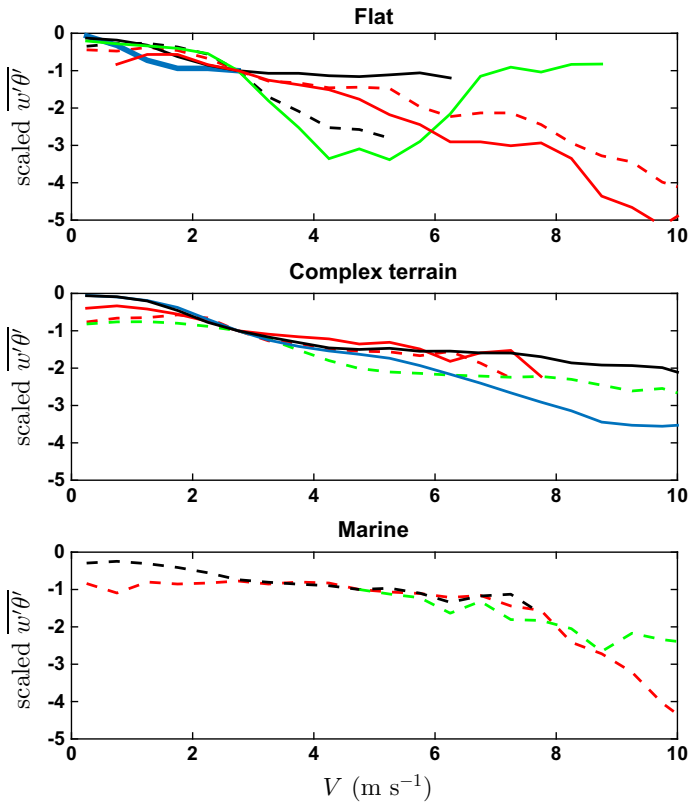
Fig. 3 Heat flux as a function of V: **a** Alaska (*red dashed*), EBEX (*black dashed*), SMACEX (*black solid*), BPP (*blue solid*, insufficient data for $V > 3$ m s^{-1}), CASES-99 (*green solid*), and Falster (*red solid*). **b** Burn (*red dashed*), Intermediate Pine (*green dashed*), Juniper (*red solid*), FLOSSII (*blue solid*), and SCP AI (*black solid*). **c** OHATS (*red dashed*), ASIT (*black dashed*) and NEAQS (*green dashed*). Heat-flux values are normalized by the value for the 2.5–3m s^{-1} interval of V to partially offset differences between sites resulting from different observational heights, data processing and surface conditions. For the windier marine sites, the heat-flux values are normalized by the mean value for the for the 4.5–5 m s^{-1} interval of V

hundred metres while the Alaska site (Pt. Barrow) is 300–400 km north of the Brooks Range. The BPP site includes low terrain rising 500 m above the site beginning a few tens of km west of the site, depending on the exact wind direction. It is not known if topographically-induced disturbances generate significant horizontal temperature advection at these sites.

For the marine sites (Fig. 3c), where the stratification is maintained mainly by warm-air advection and not by surface radiative cooling, $\delta\theta$ can increase with increasing V (Mahrt et al. 2016). As a result, the downward heat flux may increase even more rapidly with increasing V for large V as occurs in the OHATS field program.

4.2 Correlation

Interpreting the dependence of the heat flux on V is facilitated by analyzing the contributions to the right-hand side of

$$\overline{w'\theta'} = R_{w\theta}\sigma_w\sigma_\theta, \tag{8}$$
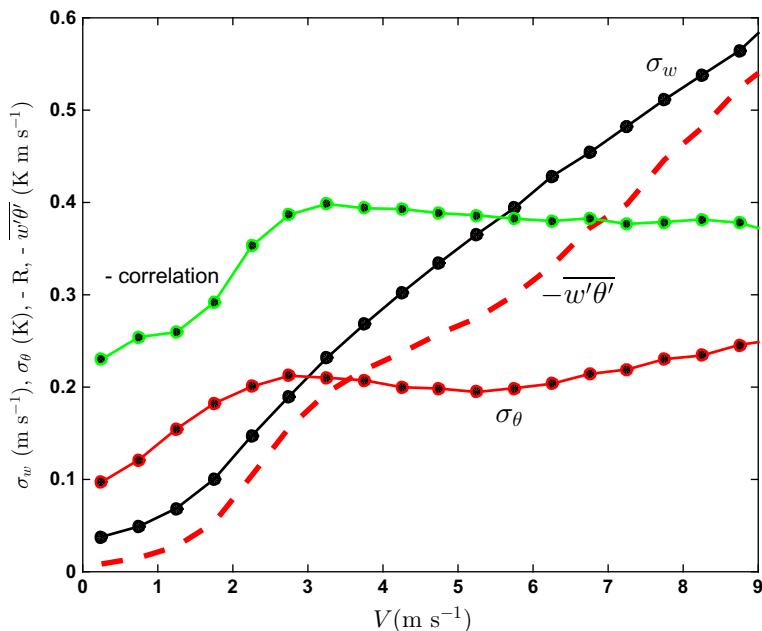
**Fig. 4** Bin-averages values of $-\overline{w'\theta'}$ (*red dashed*), σ_w (*black*), σ_θ (*red*), and the negative of the correlation coefficient $-R_{w\theta}$ (*green*) as a function of V for the FLOSSII site

where σ is the standard deviation and $R_{w\theta}$ is the correlation coefficient between the fluctuations of vertical velocity and potential temperature. For the FLOSSII measurements, the large downward heat flux for large V is aided by the systematic increase of σ_w with increasing V (black curve, Fig 4) and the maintenance of significant σ_θ with large V (red curve) associated with non-zero $\delta\theta$. Evidently, the increase in turbulence with increasing V is sufficient to generate significant temperature fluctuations even with $\delta\theta$ reduced compared to that for smaller V.

The correlation coefficient $R_{w\theta}$ is a measure of the efficiency of the heat transport, and tends to be small for weak-wind stratified conditions (Fig. 4) probably due, at least in part, to the contribution of non-turbulent motions to σ_w. As a likely result, the correlation coefficient decreases with increasing averaging time through inadvertent capture of non-turbulent motions as part of the fluctuating flow. The correlation coefficient $R_{w\theta}$ reaches an approximate constant value of -0.4 for $V > 3 \, \text{m} \, \text{s}^{-1}$ (Fig. 4). This near-constant value of $R_{w\theta}$ for large V is observed at the other sites although the dependence of $R_{w\theta}$ on V for some sites is not as systematic as in Fig. 4.

In summary, increasing heat flux for large V is maintained in spite of decreasing $\delta\theta$, because the turbulence increases with increasing V and both the efficiency of the transport ($R_{w\theta}$) and σ_θ are maintained with large V. These features are generally found at the other sites although between-site differences can be substantial.

The downward heat flux reaches a well-defined maximum at an intermediate value of the stratification (Fig. 2b) as conceptualized in Donda et al. (2016). For small values of $\delta\theta$, the temperature fluctuations are small, leading to small downward heat flux. For the largest values of $\delta\theta$, the turbulence is usually weak, leading to small downward heat flux. The downward
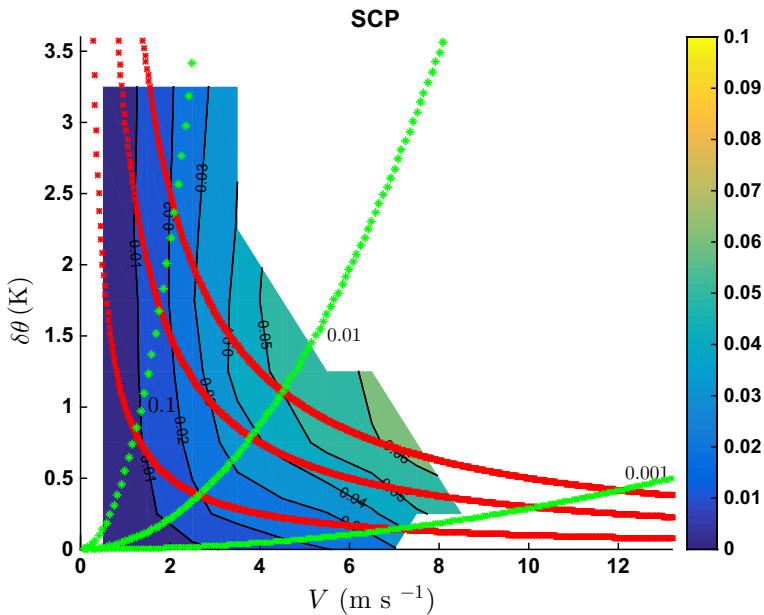
Fig. 5 The joint-average of 1-min averages of $-\overline{w'\theta'}$ for the FLOSSII measurements for intervals of $V = 1 \text{ m s}^{-1}$ and intervals of $\delta\theta = 0.5$ K. The *colour bar* identifies the magnitude of $-\overline{w'\theta'}$ in units of K m s^{-1}. The *red lines* correspond to constant values of $V\delta\theta$ corresponding to 1, 3 and 5 K m s^{-1}. The *green lines* correspond to constant values of Rb corresponding to 0.001, 0.01 and 0.1, with larger values on the *left*

heat flux reaches a maximum value for intermediate values of $V\delta\theta$ although the sample size is small for larger values of $V\delta\theta$.

4.3 Joint Dependence of Heat Flux on V and $\delta\theta$

Large downward heat flux for large V can also be examined in terms of the bivariate distribution (Williams et al. 2013) in $\delta\theta - V$ space. Within the resolution of Fig. 5, the heat flux in the FLOSSII experiment is sensitive to $\delta\theta$ only for large V where the largest values of the downward heat flux in the entire dataset are found for the most significant values of $\delta\theta$ at large V. The downward heat flux for large V becomes small for the smallest values of $\delta\theta$.

For weak winds, the downward heat flux is relatively independent of $\delta\theta$, evidently due to the competing influence of reduced vertical velocity fluctuations but increased temperature fluctuations for a given value of the turbulence intensity. For a given value of $V\delta\theta$ (red curves in Fig. 5), the averaged downward heat flux and thus C_H increase toward the right of the plot corresponding to decreasing Rb (green curves), thus following the expected role of decreasing stability. The bivariate distribution of the downward heat flux for the SCP measurements is similar but a little more ragged, probably due to the smaller dataset compared to the FLOSSII dataset.

5 Relationship of $\delta\theta$ to V and R_{net}

For $V < 2 \text{ m s}^{-1}$ (Fig. 6a), $\delta\theta$ is approximately independent of V. For $2 \text{ m s}^{-1} < V < 5 \text{ m s}^{-1}$, $\delta\theta$ decreases rapidly with increasing V presumably due to the increased turbulent
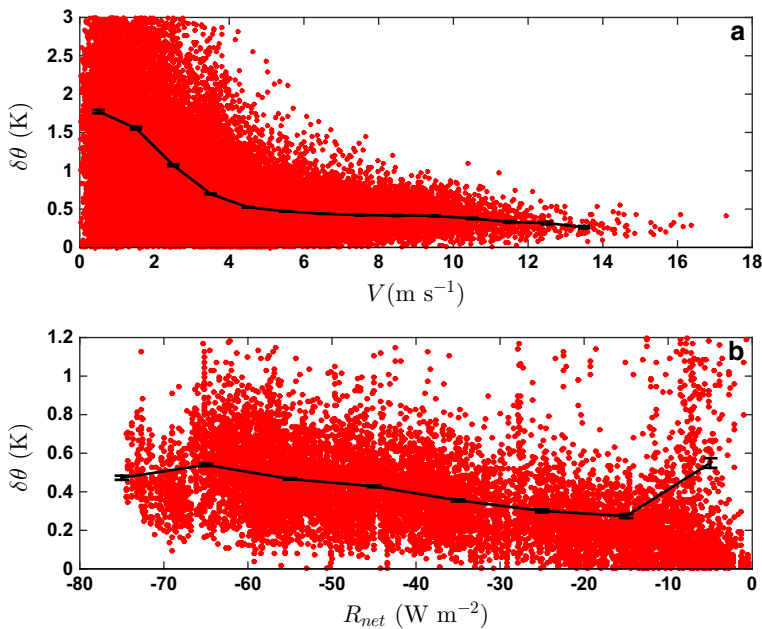
Fig. 6 **a** The dependence of $\delta\theta$ on the 1-m value of V for $-R_{net} > 20$ W m^{-2}, and **b** on R_{net} for the FLOSSII site for $V > 6$ m s^{-1}

mixing. This decrease of $\delta\theta$ is not as rapid as in recent measurements collected over a homogeneous snow surface in Antarctica (personal communication, Bas Van de Wiel and Etienne Vignon 2016). However, the decrease in $\delta\theta$ in Fig. 6a sharpens with use of V at higher levels where the wind vector is steadier. Advection of temperature and short-term variability of cloud cover probably contribute to the smoothness of $\delta\theta(V)$ in Fig. 6a. For example, the magnitude of the net radiation between subsequent 10-min periods varies by an average of 20% for the entire field program due to variable cloudiness on many of the nights.

The stratification $\delta\theta$ becomes relatively independent of V for $V > 6$ m s^{-1} (Fig. 6a), and a significant $\delta\theta$ of 0.35 K over the thin 1.5-m layer is maintained even for the interval of largest V. Significant $\delta\theta$ is also observed for large V and surface radiational cooling at the SCP site. Large V corresponds to a large advection velocity, which evidently maintains the stratification in spite of strong vertical mixing. An instrumental offset in $\delta\theta$ seems unlikely because the heat flux, averaged over bins of $\delta\theta$, vanishes for vanishing $\delta\theta$, at least within 0.1 K.

We now examine the dependence of $\delta\theta$ on R_{net} for $V > 6$ m s^{-1} where the relationship between $\delta\theta$ and V is weak. The bin-averaged values of $\delta\theta$ for the FLOSSII site increase systematically with increasing $-R_{net}$ until $-R_{net}$ reaches about 65 W m^{-2} (Fig. 6b). The cause and significance of this saturation is unknown. $\delta\theta$ is also large on cloudy nights ($-R_{net} < 10$ W m^{-2}) and is due to warm-air advection or some other unknown influence. Cloudy nights are not included in Fig. 6a because of the restriction on net radiation.

6 Dependence of $\delta\theta$ on Wind Direction for Large V

The prevailing wind direction at the FLOSSII site is south to south-west at the surface and rotates towards the west with height. Before reaching the site, south-westerly or westerly air-

flow may have passed over the north-south oriented Park Range, which commences roughly 30 km to the west of the site and rises 1000–1500 m above the tower site. Southerly flow may have occurred over Peterson Ridge, which begins a few kilometres south of the site and crests about 200 m above the site. The terrain presumably disturbs the upwind air flow, enhances downward mixing of warm air and induces the downward advection of larger potential temperature (adiabatic warming by subsidence), all contributing to higher temperatures upwind from the FLOSSII site. Such warm air might be advected over the colder surface at the FLOSSII site. On a much smaller horizontal scale for southerly or south-westerly flow, the matted grass undergoes transition to brush 100–300 m upwind, depending on the exact wind direction. Potential advection of warmer air from the rougher surface may locally contribute to the maintenance of stratification for large V, although the temperature measured over a brush site 1 km from the tower was not significantly larger for large V.

The dependence of $\delta\theta$ on wind direction and potential temperature advection for large V at the FLOSSII site is difficult to determine. This is due to a lack of measurements for wind directions other than the prevailing wind direction, and because of a correlation between wind direction and R_{net}.

The dependence of R_{net} on wind direction for large V (>6 m s^{-1}) is weaker at the SCP site compared to the FLOSSII site; and the range of wind direction is larger, allowing for a better examination of the potential influence of directionally-dependent temperature advection on $\delta\theta$. We therefore analyze the smaller SCP dataset in this section. The front range of the Rocky Mountains commences roughly 50 km to the west and rises to an altitude more than 2000 m above the SCP site. With westerly flow, this mountain range could induce increased mixing and subsidence and thus warmer air upwind, which in turn is advected over the SCP site. For example, downward heat flux is observed in strong flow over mountain ranges apparently due to strong downward mixing of overlying warmer air (e.g. Lothon et al. 2003). On average, for large V (>6 m s^{-1}), $\delta\theta$ at SCP station A1 is significant positive for westerly flow and becomes small for northerly flow that includes a mix of stable and unstable stratification (Fig. 7). The influence of net radiative cooling on $\delta\theta$ is obscure for $V > 6$ m s^{-1} presumably because of the generation of $\delta\theta$ primarily by temperature advection for large V.

Inspection of individual cases where the wind direction shifts to northerly flow with large V indicates that $\delta\theta$ tends to decrease with time after the frontal passage. This decrease is partly due to continued decreasing temperature behind the front, which also contributes to the scatter in Fig. 7. Figure 7 must be interpreted with caution because the strong northerly flow is dominated by only a few frontal passages during the 2-month field program. The results for the FLOSSII data are similar to those in Fig. 7 except that the inferred warm-air advection occurs for southerly or south-westerly flow instead of westerly flow, and the number of cases with northerly flow and inferred cold-air advection is even smaller than in the SCP measurements.

Other potential influences on $\delta\theta$ could not be established from the measurements. For example, the time series indicate that significant negative $\delta\theta$ values on time scales of 10 s to 2 min are relatively rare such that complete overturning by vigorous eddies does not seem important. Large positive $\delta\theta$ for large V could survive immediately following flow acceleration because the increased mixing requires a finite time to reduce the stratification. These events also appear to be unimportant. Cold-air advection is less likely to create a large vertical difference of potential temperature because unstable stratification enhances mixing and reduces the stratification. For both the FLOSSII and SCP sites with $V > 6$ m s^{-1}, σ_w/V increases weakly as $\delta\theta$ decreases and becomes negative, although the scatter is large (not shown).
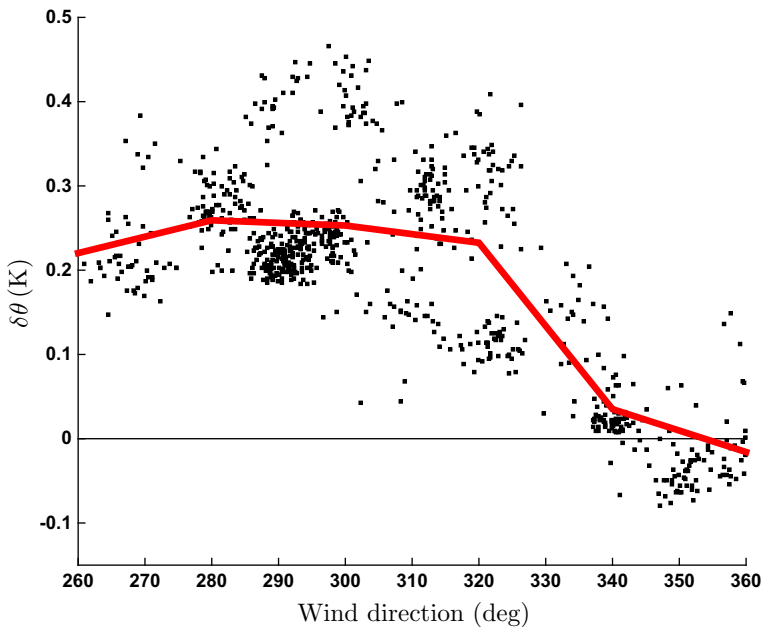
Fig. 7 The stratification $\delta\theta$ as a function of wind direction for stronger winds ($V > 6$ m s^{-1}) at SCP station A1. The *solid red line* corresponds to bin averages of all of the data over the 15° intervals of wind direction that include at least 20 points

The stratification $\delta\theta$ in the BPP and CASES-99 field programs for large V is largest for southerly flow and smallest for northerly flow. Unique to the CASES-99 site, the strongest winds are dominated by northerly flow and small $\delta\theta$, consistent with an overall decrease of the downward heat flux with increasing V in CASES-99 measurements (green line, Fig. 3a). It is not known whether warm-air advection supports the large downward heat flux for large V at the auxilliary sites where adequate measurements of $\delta\theta$ are not available (Fig. 3).

If higher topography induces warm-air advection into valleys, as suggested above, this process would explain why the downward heat flux, on average, is largest for strong winds (Fig. 3b). If flat sites with topography within 50-100 km of the site are reclassified as complex terrain sites, then only the CASES-99 and Falster sites remain classified as flat terrain (Sect. 4.1). Air located 100 km upwind from a given site with $V = 10$ m s^{-1} requires only about 3 h to reach the site. Finally, recall that positive $\delta\theta$ is maintained for large V at the marine sites by warm-air advection over cooler water.

7 Conclusions

The windy nocturnal boundary layer is found to be more complex than anticipated. The downward heat flux near the surface is large for strong winds at most of the sites considered, in contrast to the scenario of near-elimination of the stratification by strong mixing and associated reduction of the heat flux. For the sites in our study, warm-air advection appears to maintain the stable stratification in windy conditions in spite of vigorous vertical mixing. At the FLOSSII site, warm-air advection is inferred from the residual of the heat budget of the

air for strong winds and the failure of strong vertical mixing to eliminate the stratification for those wind directions where rougher surfaces and significant topography are located upwind. The SCP site also experiences significant stratification when the airflow is from an upwind mountainous region. The stratification with strong winds is smaller or even negative with northerly flow that often follows cold-frontal passages.

Warm-air advection might be frequently induced by topographically-generated turbulence and subsidence, and/or greater roughness upwind from observational sites that are located in valleys or locations with locally short vegetation. The impact of rougher surfaces and topography upwind needs to be studied more explicitly. Further progress would benefit from case studies and a much longer dataset with quality measurements of stratification, heat fluxes and the radiation components.

References

Acevedo O, Mahrt L (2010) Systematic vertical variation of mesoscale fluxes in the stable boundary layer. Boundary-Layer Meteorol 135:19–30

Acevedo O, Mahrt L, Puhales FS, Costa FD, Medeiros LE, Degrazia GA (2015) Contrasting structures between the decoupled and coupled states of the stable boundary layer. Q J R Meteorol Soc 142:693–702

Bonin TA, Blomber WG, Klein PM, Chilson PB (2015) Thermodynamic and turbulence characteristics of the southern great plains nocturnal boundary layer under differing turbulent regimes. Boundary-Layer Meteorol 157:401–420

Dellwik E, Jensen NO (2000) Internal equilibrium layer growth over forest. Theor Appl Climatol 66:173–184

Donda JMM, de Wiel BJHV, Bosveld FC, Beyrich F, van Heijst GJF, Clercx HJH (2016) The maximum sustainable heat flux in stably stratified channel flows. Q J R Meteorol Soc 142:781–792

Edson JB, Crawford T, Crescenti J, Farrar T, Frew N, Gerbi G, Helmis C, Hristov T, Khelif D, Jessup A, Jonsson H, Li M, Mahrt L, McGillis W, Plueddemann A, Shen L, Skyllingstad E, Stanton T, Sullivan P, Trowbridge J, Vickers D, Wang S, Wang Q, Weller R, Wilkin J, Williams A, Yue E, Zappa C (2007) The coupled boundary layers and air–sea transfer experiment in low winds. Bull Am Meteorol Soc 88:341–356

Edwards J (2009) Radiative processes in the stable boundary layer: part II. The development of the nocturnal boundary layer. Boundary-Layer Meteorol 131:127–146

Fairall CW, Bariteau L, Grachev AA, Hill RJ, Wolfe DE, Brewer WA, Tucker SC, Hare JE, Angevine WM (2006) Turbulent bulk transfer coefficients and ozone deposition velocity in the International Consortium for Atmospheric Research into Transport and Transformation. J Geophys Res 111:D23S20. doi:10.1029/2006JD007597

Garratt JR (1990) The internal boundary layer: a review. Boundary-Layer Meteorol 50:171–203

Hoch SW, Calanca P, Philipona R, Ohmura A (2007) Year-round observation of longwave radiative flux divergence in Greenland. J Appl Meteorol Climatol 46:1469–1479

Kelly M, Wyngaard JC, Sullivan PP (2009) Application of a subfilter-scale flux model over the ocean using OHATS field data. J Atmos Sci 136:3217–3225

Kustas W, Li F, Jackson J, Preuger J, MacPherson J, Wolde M (2004) Effects of remote sensing pixel resolution on modeled energy flux variability of croplands in Iowa. Remote Sens Environ 92:535–547

Lothon M, Druilet A, Bénech B, Campistron B, Bernard S, Saïd F (2003) Experimental study five föhn events during the mesoscale alpine programme: from synoptic scale to turbulence. Q J R Meteorol Soc 129:2171–2193

Mahrt L, Thomas CK (2016) Surface stress with non-stationary weak winds and stable stratification. Boundary-Layer Meteorol 159:3–21

Mahrt L, Vickers D (2005) Boundary-layer adjustment over small-scale changes of surface heat flux. Boundary-Layer Meteorol 116:313–330

Mahrt L, Thomas CK, Preuger J (2009) Space-time structure of mesoscale modes in the stable boundary layer. Q J R Meteorol Soc 135:67–75

Mahrt L, Andreas EL, Edson JB, Vickers D, Sun J, Patton EG (2016) Coastal zone surface stress with stable stratification. J Phys Oceanogr 46:95–105

Nakamura R, Mahrt L (2006) Vertically-integrated sensible heat budgets for stable nocturnal boundary layers. Q J R Meteorol Soc 132:383–403

Oliveira PES, Acevedo OC, Moraes OLL, Zimermann HR, Teichrieb C (2012) Nocturnal intermittent coupling between the interior of a pine forest and the air above it. Boundary-Layer Meteorol 146:45–64

Oncley SP, Foken T, Vogt R, Kohsiek W, de Bruin H, Bernhofer C, Christen A, van Gorsel E, Grantz D, Lehner I, Liebethal C, Liu H, Mauder M, Pitacco A, Ribeiro L, Weidinger T (2007) The energy balance experiment ebex-2000. Part 1: overview and energy balance. Boundary-Layer Meteorol 123:1–28

Poulos G, Blumen W, Fritts D, Lundquist J, Sun J, Burns S, Nappo C, Banta R, Newsome R, Cuxart J, Terradellas E, Balsley B, Jensen M (2001) A comprehensive investigation of the stable nocturnal boundary layer. Bull Am Meteorol Soc 83:555–581

Schwarz P, Law B, Williams M, Irvine J, Kurpius M, Moore D (2004) Climatic versus biotic constraints on carbon and water fluxes in seasonally drought-affected ponderosa pine ecosystems. Glob Change Biol 18:1029–1037

Sterk HAM, Steeneveld GJ, Bosveld FC, Vihma T, Anderson PS, Holtslaga AAM (2016) Clear-sky stable boundary layers with low winds over snow-covered surfaces. Part 2: process sensitivity. Q J R Meteorol Soc 142:821–835

Stoll R, Porté-Agel F (2009) Surface heterogeneity effects on regional-scale fluxes in stable boundary layers: surface temperature transitions. J Atmos Sci 15:1392–1404

Sun J (2007) Tilt corrections over complex terrain and their implication for CO_2 transport. Boundary-Layer Meteorol 124:143–159

Sun J, Burns S, Lenschow D, Banta R, Newsom R, Coulter R, Frasier S, Ince T, Nappo C, Cuxart J, Blumen W, Lee X, Hu XZ (2002) Intermittent turbulence associated with a density current passage in the stable boundary layer. Boundary-Layer Meteorol 105:199–219

Sun J, Mahrt L, Banta RM, Pichugina YL (2012) Turbulence regimes and turbulence intermittency in the stable boundary layer during CASES-99. J Atmos Sci 69:338–351

Sun J, Lenschow DH, Mahrt L, LeMone MA, Mahrt L (2016) The role of large-coherent-eddy transport in the atmospheric surface layer based on CASES-99 observations. Boundary-Layer Meteorol 160:83–111

Thomas CK, Kennedy A, Selker J, Moretti A, Schroth M, Smoot A, Tufillaro N (2012) High-resolution fibre-optic temperature sensing: a new tool to study the two-dimensional structure of atmospheric surface-layer flow. Boundary-Layer Meteorol 142:177–192

Van de Wiel BJH, Moene AF, Jonker HJJ, Baas P, Basu S, Donda JJM, Sun J, Holtslag AAM (2012) The minimum wind speed for sustainable turbulence in the nocturnal boundary layer. J Atmos Sci 69:3116–3127

Van Hooijdonk I, Donda J, Clercx H, Bosveld F, de Wiel BV (2015) Shear capacity as prognostic for nocturnal boundary layer regimes. J Atmos Sci 72:1518–1532

Vickers D, Mahrt L (2006) Contrasting mean vertical motion from tilt correction methods and mass continuity. Agric For Meteorol 138:93–103

Vosper S, Hughes JK, Lock AP, Sheridan PF, Ross AN, Jemmett-Smith B, Brown A (2013) Cold-pool formation in narrow valleys. Q J R Meteorol Soc 127:429–448

Williams A, Chambers S, Griffiths S (2013) Bulk mixing and decoupling of the stable nocturnal boundary layer characterized using a ubiquitous natural tracer. Boundary-Layer Meteorol 149:381–402